energies

MDPI

Article

Aerothermal Investigation of the Effect of Endwall Structures on Radial Turbine Heat Losses

M. A. Khader [1,*], A. I. Sayma [2], Jafar Al-Zaili [3], Mohsen Ghavami [3] and Hongwei Wu [1]

[1] Department of Mechanical Engineering, University of Hertfordshire, College Lane, Hatfield AL10 9AB, UK; h.wu6@herts.ac.uk
[2] Department of Mechanical Engineering, Brunel University London, Kingston Lane, London UB8 3PH, UK; abdulnaser.sayma@brunel.ac.uk
[3] Department of Engineering, City St George's, University of London, Northampton Square, London EC1V 0HB, UK; jafar.alzaili@city.ac.uk (J.A.-Z.); m.ghavami@city.ac.uk (M.G.)
* Correspondence: m.khader@herts.ac.uk

Abstract

This paper presents a detailed numerical investigation of the effect of hub-mounted riblets on the thermal and aerodynamic performance of a radial turbine rotor. While prior studies have shown that riblets reduce wall shear stress and improve aerodynamic efficiency, their influence on heat transfer and thermal losses remains underexplored. Using numerical simulations, this study examines the heat transfer characteristics within the rotor passage, comparing ribbed and smooth hub configurations under the same operating conditions. Results reveal that although riblets reduce frictional drag, they also enhance convective heat transfer—leading to a 6% increase in the heat transfer coefficient at the hub and 2.8% at the blade surfaces. This intensification of heat transfer results in a 4.3% rise in overall thermal losses, counteracting some of the aerodynamic gains. The findings provide new insights into the thermofluidic implications of surface modifications in turbomachinery and emphasise the importance of considering surface finish not only for aerodynamic optimisation but also for thermal efficiency. These results can inform future turbine design and manufacturing practices aimed at controlling surface roughness to minimise heat loss.

Keywords: riblets; radial turbine; heat transfer; shear stress reduction; micro gas turbines

check for updates

Received: 15 July 2025
Revised: 7 August 2025
Accepted: 14 August 2025
Published: 16 August 2025

Citation: Khader, M.A.; Sayma, A.I.; Al-Zaili, J.; Ghavami, M.; Wu, H. Aerothermal Investigation of the Effect of Endwall Structures on Radial Turbine Heat Losses. *Energies* **2025**, *18*, 4366. https://doi.org/10.3390/en18164366

Copyright: © 2025 by the authors. Licensee MDPI, Basel, Switzerland. This article is an open access article distributed under the terms and conditions of the Creative Commons Attribution (CC BY) license (https://creativecommons.org/licenses/by/4.0/).

1. Introduction

Over the past two decades, there has been significant attention directed toward the development of micro gas turbines (MGTs). This growing interest stems from the need for compact, efficient, and reliable power generation solutions, particularly in off-grid areas where traditional power infrastructure is unavailable. Micro gas turbines offer a versatile energy source for a range of applications, such as remote communities, emergency backup power, and mobile power units. Their compact size and modular design make them ideal for use in portable power systems, range extenders for electric vehicles, autonomous robots, and military operations where flexibility and mobility are critical [1,2]. One of the key advantages of micro gas turbines is their capability to support distributed power generation, which enhances energy resilience by reducing reliance on centralised grids. Moreover, micro gas turbines (MGTs) can be incorporated into combined heat and power (CHP) systems, generating both electricity and usable thermal energy in a single process. This dual-output approach substantially enhances overall energy efficiency. This makes them an attractive solution for commercial and residential buildings, as well as industrial

applications where both power and heat are required [3]. Furthermore, micro gas turbines are well-suited for fuel-flexible power generation, capable of operating on a wide variety of fuels, including natural gas, biogas, hydrogen, and even liquid fuels. This adaptability is particularly advantageous in the context of transitioning to cleaner energy sources, as MGTs can run on renewable fuels like biofuels and hydrogen with minimal modifications. Additionally, integrating micro gas turbines with renewable energy sources such as solar can provide hybrid systems that further enhance energy security and sustainability [4,5].

Despite that, large gas turbines used in power generation can achieve high efficiencies, MGTs still suffering from low efficiency. This came as a result of size reduction which led to reduce the performance of the turbomachinery components, limits the maximum operating temperature to the material limits in the absence of cooling to the blades of the turbine and the increase in the thermal loss from the turbine side to the other components of the MGT due to size restrictions and shaft arrangement. The aerodynamic efficiency penalty arises from several factors: shorter blade heights, tighter machining tolerances, increased clearance-to-blade-height ratios, and the challenges of low Reynolds number operation. The latter exacerbates losses by elevating skin friction and heat transfer effects [6–8].

Riblets are surface structures with different shapes and arrangements, where they are normally arranged such that the grooves between them are parallel to the blades. These structures were initially inspired by the riblets found on shark skin, where they proved to reduce their body drag during swimming [9]. Later, those structures started to be implemented in industrial applications in an attempt to improve the aerodynamic performance of certain components, such as aeroplane wings. The coming literature review sheds light on the previous studies performed to identify the effect of riblets on drag in different applications.

Walsh [10] experimentally demonstrated that V-groove riblets applied to a flat plate can achieve up to 8% drag reduction, with performance varying across different riblet geometries and dimensional parameters. And on a different application, Kim et al. [11] and Miao et al. [12] fabricated different shapes and sizes of riblets on the endwall of 90° turning ducts with a rectangular cross-section to investigate their ability to reduce the secondary flow generation within the mainstream flow. As a result, they found that adding riblets alleviates the size of the streamwise vortex and has a positive effect on reducing the pressure drop along the ducts.

Oehlert et al. [13] and Zhong et al. [14] tested the effect of adding riblets at the hub surface of an axial compressor cascade hub. The analysis revealed that fence-crossflow interaction effectively suppresses secondary flow by generating counter-rotating vortical structures. These opposing vortices weaken the primary passage vortex, thereby reducing vertical fluid oscillations. This flow modification subsequently decreases wall shear stress and skin friction drag.

Zhang et al. [15] and Govardhan et al. [16] investigated the application of engineered riblets on axial turbine hub surfaces to enhance aerodynamic performance. Their findings demonstrated that riblet structures effectively attenuate both the pressure-side leg of the horseshoe vortex and the subsequent development of the passage vortex. This flow control mechanism reduces turbulent mixing within the turbine passage, thereby decreasing the overall pressure drop and improving turbine efficiency. The application of riblets has been extended to radial inflow turbines through investigations by Khader et al. [17,18]. Their studies examined cusp-shaped riblets with varying heights and spacings on rotor hubs, demonstrating that these surface modifications reduce hub wall shear stress by suppressing cross-stream motion of low-momentum fluid. This suppression limits streamwise vortex interaction with the hub surface. However, the riblet-crossflow interaction generates secondary flow structures that increase passage pressure losses. Notably, the net effect

proves aerodynamically beneficial when riblet heights are maintained below 19.3 wall units, as this configuration optimally balances shear stress reduction against secondary flow losses.

The application of riblets was not only limited to reducing the aerodynamic losses, but also it was used to manipulate the heat transfer coefficient near the surface in certain applications. The following studies studied the effect of riblets on enhancing the heat transfer between the surfaces and the surrounding fluid. Camci et al. [19] studied the effect of adding a single blade-shaped riblet on the heat transfer near the endwall of a 90° turning duct. In his experiment, he compared the values of the convective heat transfer coefficient over a smooth surface and a surface with a riblet located at the mid distance between the pressure and the suction surfaces of the duct. The comparison included different riblet heights and widths. For all cases, the endwall heat transfer was enhanced up to 30% compared to the smooth wall.

In more recent studies, Miao et al. [20,21] investigated the ability of riblets to improve the film-cooling effectiveness of an axial turbine rotor hub. The investigation was carried out experimentally and numerically, comparing the purged flow cooling effectiveness over a smooth surface and a surface with riblets. Both computational analysis and experiments confirmed the ability of riblets to improve the heat transfer coefficient near the endwall, leading to better cooling effectiveness.

Wang et al. [22,23] studied numerically the effect of adding wavy riblets to the end walls of straight and U-shaped channels mimicking the cooling channels used in the axial turbine blades. The results showed an improvement in the heat transfer rate through the walls with riblets, while the heat transfer rate through the smooth side walls is reduced as riblets limit the congestion of the secondary flows close to the side walls of the channels. As an overall result, the heat transfer improved by up to 30%.

Kaewchoothong et al. [24] studied the effect of riblet arrangement on the heat transfer coefficient in a stationary channel that mimics the cooling channels in axial turbomachinery blades. This study revealed that the arrangement of the riblets has a strong impact on the local heat transfer coefficient, where the latter can be improved by around 32% by optimising the angle of the riblets relative to the mainstream flow direction. Building on this theme, Davletshin et al. [25] investigated the enhancement of convective heat transfer by covering a channel wall with regularly spaced, small-sized ribs through combined experimental measurements and CFD simulations. Their study demonstrated that these ribs generate streamwise and secondary vortices that disrupt the thermal boundary layer, intensify fluid mixing near the wall, and elevate local turbulence levels, leading to a substantial rise in wall heat transfer. Detailed flow visualisations confirmed that rib-induced vortical structures break up thermal gradients, contributing to an increase in both local and average Nusselt numbers. Extending the analysis to annular geometries, Mantri and Abraham [26] conducted experimental and numerical investigations to evaluate the impact of rib turbulation on heat transfer and flow characteristics within the annular space of a double-pipe heat exchanger. Their study demonstrated that the introduction of ribs in the annulus induces secondary flows and enhances turbulence, leading to a significant disruption of the thermal boundary layer. This disruption results in improved convective heat transfer rates.

The thermal effects of riblet surfaces in rotating machinery remain poorly understood, particularly in radial turbine applications where wall heat transfer directly influences operational efficiency. While riblets have been extensively investigated for aerodynamic modifications, their impact on thermal boundary layer development under rotating conditions has not been systematically examined. In this study, the alteration of wall heat transfer behaviour by riblet textures is investigated through comparative analysis of smooth and

modified rotor surfaces. The fundamental modifications to near-wall turbulence structures and thermal transport mechanisms are characterised, with particular attention given to the net influence on turbine thermal performance. It is demonstrated that while local heat transfer enhancement occurs at riblet-modified surfaces, this is accompanied by increased overall thermal losses—a paradoxical outcome that persists even when aerodynamically optimised geometries are employed. These findings challenge established assumptions regarding surface texturing applications in turbomachinery.

2. Geometric Definition and Turbine Configuration

Recent investigations by the authors [17,18] examined the influence of residual surface structures on radial turbine performance. The studies identified riblet height as the primary geometric parameter affecting performance, with inter-riblet spacing demonstrating only a marginal impact. Optimal performance enhancement was achieved using riblets measuring 1.5% of the rotor inlet blade height (0.06 mm). Based on these findings, such riblets were applied to the hub surface of a 6 kWe micro gas turbine rotor to evaluate their effect on passage heat transfer characteristics. The turbine stage was subsequently analysed numerically at design point conditions (Table 1), with Figure 1 illustrating the key rotor dimensions. The effects of the residual surface structures on the radial turbine's performance. They found that the main geometrical parameters that affect the riblets' performance are the height of the riblets, while the spacing between them has a marginal effect on their performance. Additionally, it was found that riblets with a height of 1.5% of the rotor inlet blade height have the largest benefit on the turbine performance. Therefore, riblets of height 0.06 mm (1.5% of the rotor inlet blade height) were introduced to the hub surface of a turbine rotor designed for a 6 kWe micro gas turbine to study their effect on heat transfer within the rotor passage. The turbine stage was then analysed numerically at design point operating conditions listed in Table 1. The main dimensions of the turbine rotor are shown in Figure 1.

Table 1. Design point specifications of the radial turbine.

		Unit
Total pressure ratio	3.0	-
Inlet total temperature	1073	K
Mass flow rate	0.09	kg/s
Output power	21	kW
Rotational speed	130,000	rpm

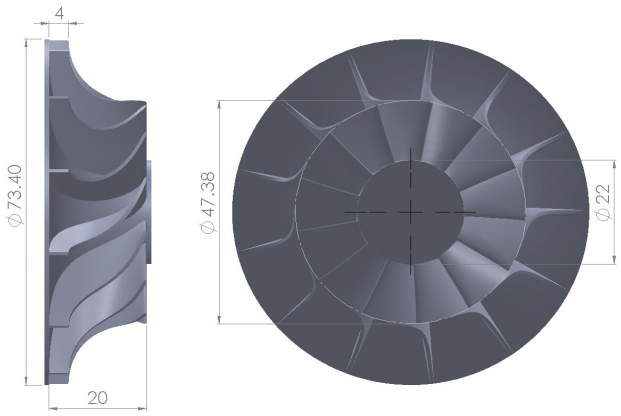

Figure 1. Rotor dimensions [mm].

This study employed the dimensionless parameter (h_{rel} = h/b) to characterise riblet height, where h represents the cusp height and b denotes the rotor inlet blade height (see Figure 2). The inter-riblet spacing (s) was designed with a convergent profile, progressively decreasing along the flow passage from inlet to outlet. Thus, the polar angle (∅) between riblets was kept constant, and the spacing s was calculated at a certain radius from Equation (1). Table 2 contains the dimensions of the riblets used in this study.

$$s = r_{hub}\varnothing \quad (1)$$

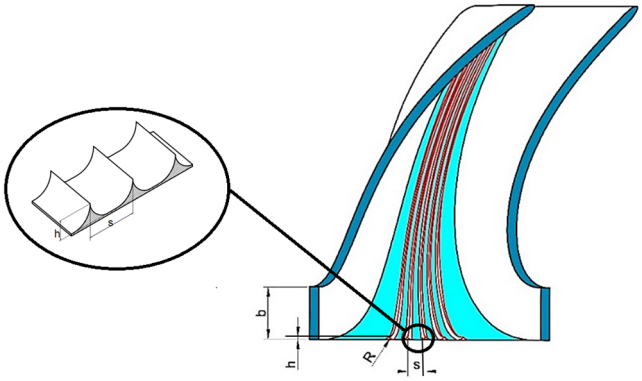

Figure 2. Riblets terminology.

Table 2. Geometric parameters of cusp-shaped riblets.

Height (h) [mm]	Relative Height (h_{rel}) [mm]	Radius (R) [mm]	Spacing (s) [3 Riblets] ∅ = 4.45°
0.06	1.5%	0.8	0.078 rhub

3. Conjugate Heat Transfer Analysis and CFD Methodology

To understand the effect of riblets on the aero-thermal performance of the turbine, we conducted a conjugate heat transfer (CHT) analysis, which will allow us to evaluate the change in the heat flux through the hub surface when riblets are added, alongside studying the effect of riblets on the heat transfer coefficient along the hub surface. The computational domain consists of fluid and solid domains. The fluid domain comprises a single rotor passage of the turbine, and the solid domain consists of a 1/13th of the turbine rotor, shaft, and 1/8th of the compressor impeller.

The fluid domain was discretized using unstructured meshing techniques implemented in ANSYS Workbench, with separate computational grids generated for both the baseline smooth hub configuration and the modified riblet-equipped geometry. Consistent meshing methodologies were applied to the solid domain components using the same software framework. Numerical solutions were obtained through ANSYS CFX 2025 R1, a commercial computational fluid dynamics solver employing Reynolds-Average Navier–Stokes (RANS) methodology. The finite volume discretisation scheme was utilised throughout the solution domain. At the rotor inlet section, the flow conditions corresponded to a Reynolds number of 27,000, calculated using the passage hydraulic diameter as the characteristic length scale. This Reynolds number value confirmed turbulent flow conditions, leading to the specification of 5% turbulence intensity at the domain inlet. This turbulence parameter selection was informed by the experimental work of Dai et al. [27], whose measurements established 7% as the upper bound for turbulence intensity in comparable rotor passages.

For turbulence closure, the k-epsilon model was implemented based on the recommendations provided by Miao et al. [20] for similar turbomachinery applications. The solver's

conjugate heat transfer capabilities enabled simultaneous resolution of fluid dynamics and solid heat conduction phenomena. Within solid regions, thermal energy transport was governed by the fundamental energy conservation equation, with heat transfer occurring exclusively through conduction mechanisms.

All passage surfaces in the fluid domain were modelled with no-slip wall boundary conditions. To ensure proper resolution of near-wall flow features, the non-dimensional wall distance (y+) was maintained below unity throughout the computational domain. A stage interface with mixing plane treatment was implemented between rotor and stator components, where circumferentially averaged flow quantities were transferred across the interface while preserving conservation laws. The computational model employed the boundary specifications in Table 3:

Table 3. MGT components' boundary conditions.

Boundary Condition	Value	Component
Inlet total pressure	2.92 (bar)	Turbine
Inlet total temperature	1073 (K)	
Outlet static pressure	1 (bar)	
Mass flow rate	0.09 (kg/s)	
Wall surface temperature	333 (K)	Compressor
Wall heat transfer coefficient	1000 (w/m^2)	
Turbine side-bearing temperature	383 (K)	Bearing contact surface of the shaft
Compressor side-bearing temperature	343 (K)	

The steady-state solution was obtained by iterating the coupled flow equations to convergence using ANSYS CFX's implicit solver. Convergence was achieved when all residual monitors showed asymptotic behaviour and key performance parameters (mass flow, efficiency) exhibited variations below 0.1% over successive iterations.

3.1. Mesh Independence Verification

A comprehensive grid convergence study was conducted to ensure numerical solutions were independent of mesh resolution. The verification process examined both fluid and solid domains separately using the following methodology.

For the fluid domain analysis, five systematically refined grids were evaluated by monitoring:

- Mass flow rate variations at the inlet and outlet sections;
- Absolute velocity profiles at key monitoring planes;
- Pressure distribution along the passage walls.

The solid domain verification employed a fixed temperature boundary condition on the turbine rotor surface while comparing the heat flux magnitude through the compressor impeller surface and the temperature gradients in critical structural components.

Mesh densities were progressively increased until variations in all monitored parameters fell below 1% relative to the finest grid solution. This rigorous validation process confirmed that further refinement produced negligible changes in solution accuracy.

The final validated mesh configurations are presented in Table 4, which includes quantitative mesh statistics such as element counts and quality metrics, Figure 3, which visualises the fluid domain mesh, and Figure 4, which illustrates the solid domain discretisation details.

Table 4. Mesh statistics for the MGT components.

Component	Nodes
Turbine fluid domain (smooth hub)	2,911,452
Turbo shaft solid domain (smooth hub)	753,915
Turbine fluid domain (hub with riblets)	3,315,606
Turbo shaft solid domain (hub with riblets)	833,919

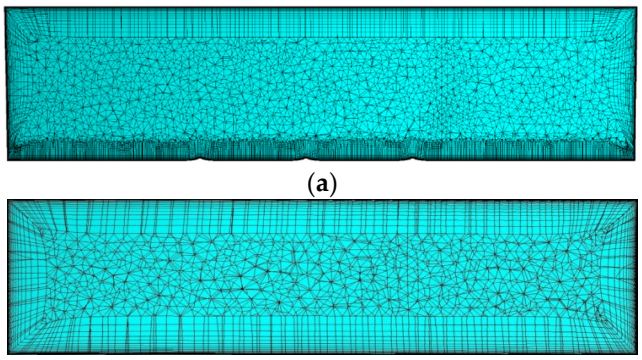

Figure 3. Computational grid: (**a**) rotor passage with riblets, (**b**) rotor passage without riblets.

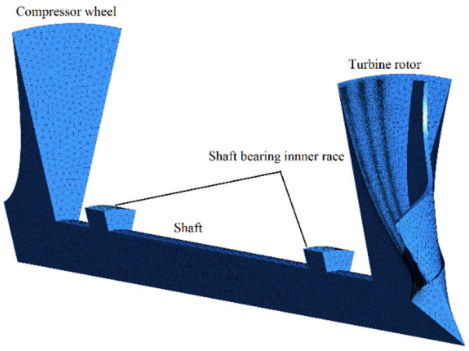

Figure 4. Solid domain unstructured mesh used in the analysis.

3.2. CFD Methodology Validation Against Experimental Data

To ensure the reliability of computational fluid dynamics (CFD) results in predicting heat transfer in turbine passages, a validation exercise was conducted using experimental data obtained from a curved duct configuration [28]. The construction of the test rig used in this study consists of a square cross-sectional duct with a 90° turning section. The duct has a width of 20.3 cm and a radius ratio of 2.3, which is defined as the mean radius divided by the duct width. The geometry of the duct is illustrated in Figure 5. The test section is located downstream of an open-loop wind tunnel, which includes an axial air blower, diffuser with multiple screens, plenum chamber, circular nozzle, circular-to-square transition nozzle, and a constant cross-sectional duct.

Although this geometry does not include riblets, it serves as a rigorous benchmark for near-wall flow physics critical to riblet performance. The duct's curvature induces Dean vortices, which are analogous to the cross-stream vortices manipulated by riblets in turbulent boundary layers, thereby validating our model's ability to capture secondary flow effects. Additionally, the high Reynolds number (Re = 360,000) ensures a turbulent flow regime representative of similar turbine environments.

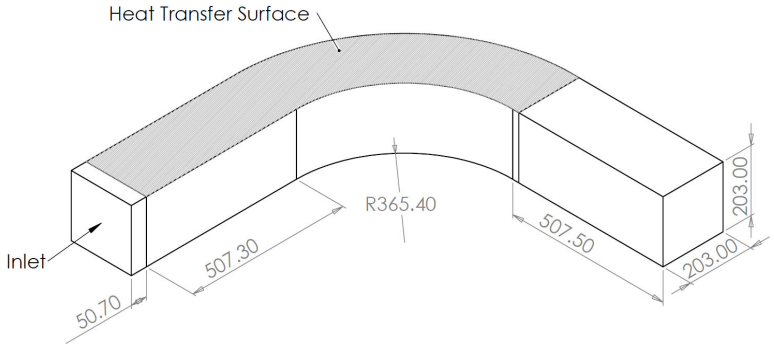

Figure 5. Geometry of test section used in validation study.

The experimental setup includes a steady-state heat transfer measurement surface constructed from a composite of an acrylic endwall (12.7 mm thick), double-sided tape (0.110 mm thick), and Inconel 600 foil (0.0254 mm thick). The surface was further coated with multiple layers of black paint and chiral nematic liquid crystals, which were used for temperature mapping during heat transfer analysis. During the experiments, the flow conditions were set to a Reynolds number of 360,000, which was calculated using the inlet centreline velocity (28.3 m/s), duct width, and ambient free-stream temperature.

Heat transfer measurements were conducted using liquid crystal thermography to determine surface temperatures. A finite element method was used to calculate the heat flux distribution on the heat transfer surface. The boundary conditions for the heat flux calculation involved a uniform potential at the bus bar and heater foil junctions and zero current flux normal to the unbounded streamwise edges (refer to [28] for a full description of the experimental setup).

The experimental results (refer to Figure 6a) consistently showed characteristic heat transfer patterns associated with secondary flow development in curved geometries. A distinct increase in heat transfer along the outer wall of the bend, caused by centrifugal forces and associated secondary vortices, was evident in both experimental representations. The inner wall, in contrast, exhibited comparatively lower heat transfer coefficients, aligning with the expected fluid dynamic behaviour.

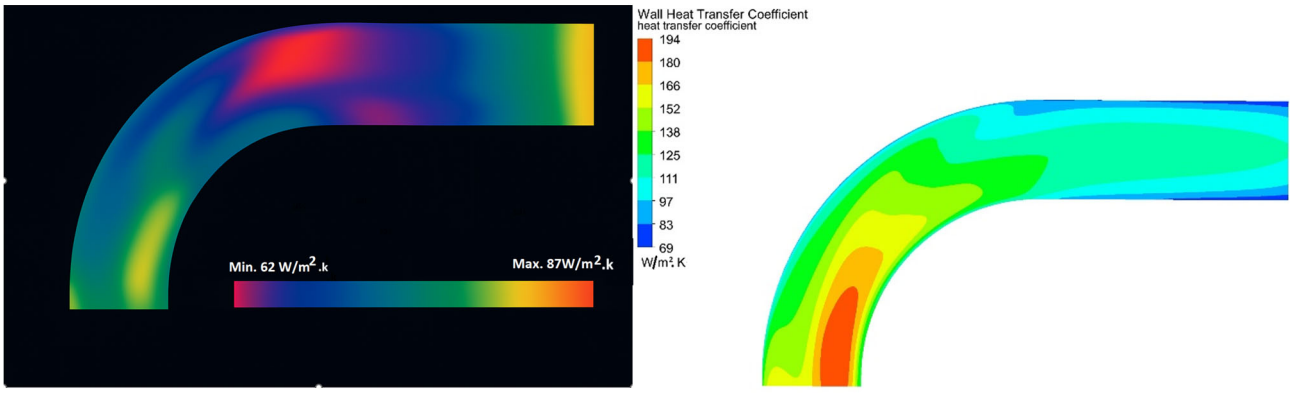

(**a**) (**b**)

Figure 6. Wall heat transfer coefficient: (**a**) experimentally estimated wall heat transfer coefficient contours (recreated from [28]), (**b**) wall heat transfer coefficient contours generated from CFD results.

The CFD simulation, employing the Reynolds-Average Navier–Stokes (RANS) approach with a standard k–ε turbulence model, was able to reproduce these key qualitative trends (refer to Figure 6b). The location and shape of the high-heat-transfer regions along the outer bend matched those seen in the experimental datasets. This indicates that the

model successfully captured the dominant flow structures responsible for heat transfer enhancement.

In terms of spatial resolution and gradient representation, the CFD results showed smoother transitions and slightly broader high-heat-transfer zones compared to the experimental colour map. This is likely due to the known diffusion characteristics of the k–ε model and the inherent averaging in RANS simulations. While some fine-scale details observed in the experimental contours were less distinct in the CFD output, the major flow phenomena and thermal behaviour were adequately captured.

Overall, the CFD model demonstrated good agreement with experimental observations in both the magnitude and distribution of wall heat transfer. It reliably captures the primary thermal and fluid dynamic features and can be confidently applied to investigate similar configurations, such as the turbine passage that is the focus of this study.

4. Results and Discussion

To study the effect of adding riblets over the hub surface on the heat transfer performance within the rotor passage, it is necessary to understand the flow characteristics there and how riblets affect the flow behaviour close to the passage surfaces.

4.1. Flow Characteristics Along the Rotor Passage and Riblets' Effect on the Secondary Flow

In this study, we will focus on the flow within the rotor passages, which is the area confined between two consecutive blades. During the operation of the turbine, the flow enters the passages almost radially towards the axis of rotation. In this section, Coriolis acceleration has the dominant effect on the secondary fluid near the passage walls. Therefore, the tendency of the low-momentum fluids is to move from the pressure surface (PS) to the suction surface (SS), where the reduced static pressure ($P_r = P_s - \frac{1}{2}\rho\omega^2 r^2$) is minimum. The length of the section depends on the design of the rotor, where low specific speed rotors have a longer radial section than high specific speed ones (see Figure 7).

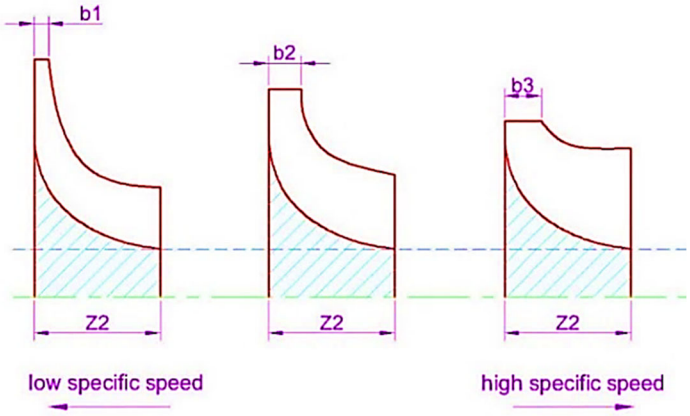

Figure 7. Radial turbine rotor with different specific speeds.

After passing the inlet section, the flow enters the bend section, where the flow tends to change direction from radial to axial. In the section, the low-momentum fluid starts to move from the PS to the suction surface due to the Coriolis force and from hub to shroud to compensate for the reduction in the rotation radius due to the bend happened to the passage [1]. At the outlet section of the rotor, the curvature of the passage tangentially increases. This drives secondary flow at the hub and shroud towards the SS towards the smaller radius of curvature. Meanwhile, Coriolis forces still drive the low-momentum fluids near the PS and SS radially towards the shroud. The secondary flow motion at each section along the rotor is summarised in Figure 8.

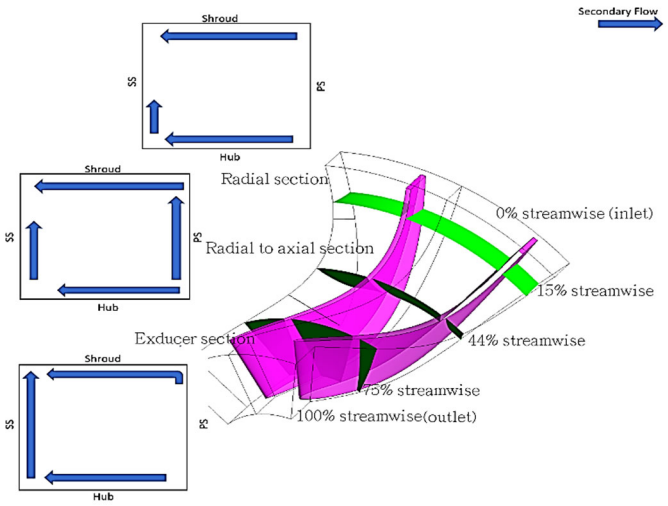

Figure 8. Secondary flow directions at 15% (developing), 44% (interacting), and 75% (exiting) axial positions.

This motion of low-momentum fluid driven by different mechanisms is the main source of passage vortices generation. To have a better understanding of the development of the passage vortical structures, λ_2 criterion was used in Figure 9 to generate a full visualisation surface for the vortices at surfaces located at 15%, 44%, and 75% of the streamwise length of the fluid domain of the rotor, as shown in Figure 9.

Figure 9a shows the passage vortices at a section located 15% of the passage streamwise length from the rotor inlet. The flow structure along this section represents a sample of the flow structure within the rotor passage radial section (see Figure 7). The vortices at the hub and shroud are mainly the result of the Coriolis acceleration effect on the low-momentum fluid, while those vortices at the corners are the result of the incidence of the incoming flow with rotor blades.

As the flow travels further down (Figure 9b,c), the vortices at the passage bottom corners getting weaker while the ones at the shroud corner, where the reduced static pressure is the lowest, gets stronger as the low-momentum fluid accumulates there. In Figure 10, the reduced static pressure contours have been plotted at the same sections as in Figure 9. The pressure contours explain the accumulation of the passage vortices in the suction side shroud corner, as the static pressure with regards to the rotating passage is the lowest at that area along the passage length. On the other hand, the pressure is highest at the opposite corner (hub pressure side corner) where the vortices vanish towards the end of the passage.

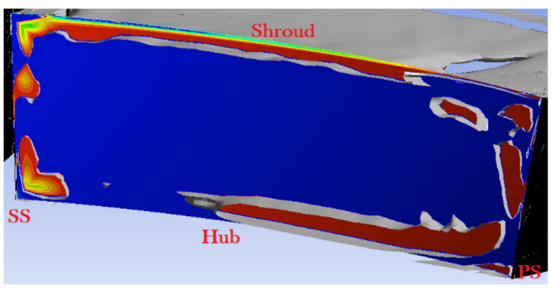

(**a**) 15% of streamwise length of the rotor passage

Figure 9. *Cont.*

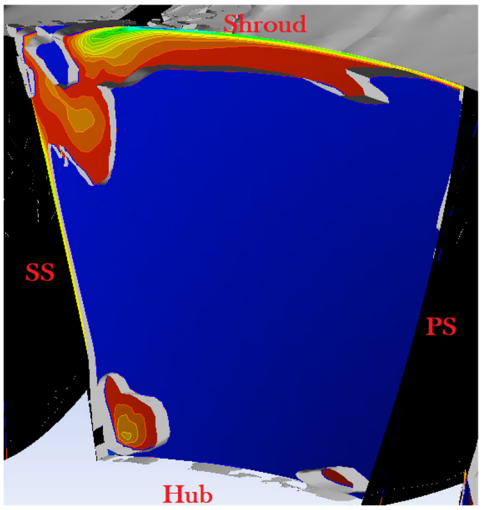

(**b**) 44% of streamwise length of the rotor passage

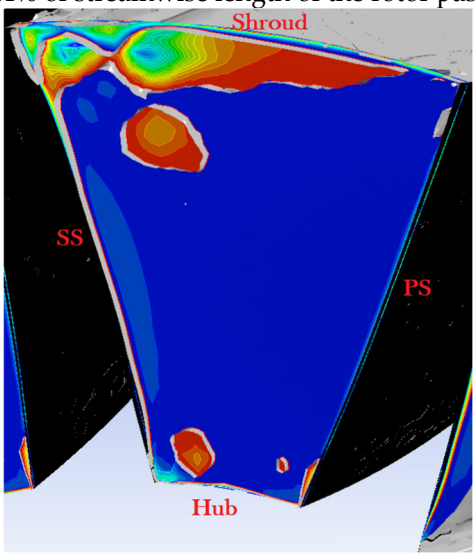

(**c**) 75% of streamwise length of the rotor passage

Figure 9. Iso surfaces of λ_2 at a different section within a rotor passage.

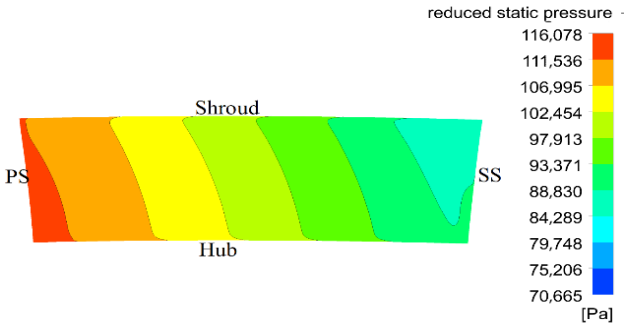

(**a**) 15% of streamwise length of the rotor passage

Figure 10. *Cont.*

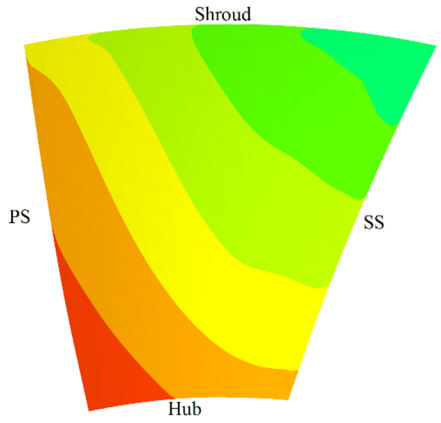

(**b**) 44% of streamwise length of the rotor passage

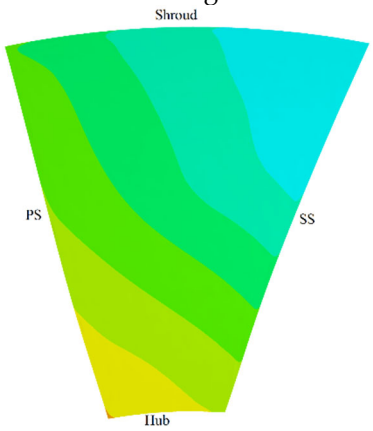

(**c**) 75% of streamwise length of the rotor passage

Figure 10. Reduced static pressure contours.

By focusing on the radial section of the passage, we found that the strong pressure gradient between the blades and Coriolis forces drives the low-momentum fluid from the pressure side to the suction side of the passage, as shown in Figure 11. By placing riblets on the hub surface, this motion is reduced, and the fluid kinetic energy within the valley drops, leading to a reduction in the momentum transfer within the boundary layer and a drop in the wall shear. The benefit of having the riblets at the rotor hub surface has been previously investigated thoroughly by the authors (please refer to [17]). Nonetheless, riblets, as discussed in the Introduction, have been reported to improve the heat transfer at the surfaces where it was attached. In the next section, the effect of riblets on the heat transfer along the rotor passage will be explored.

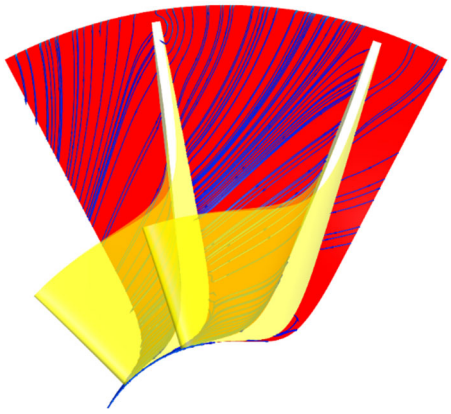

Figure 11. Limiting streamlines at the rotor hub.

4.2. Hub Heat Transfer

To study the effect of riblets on heat transfer along the hub surface, steady-state conjugate heat transfer analysis was performed for the case of a smooth hub rotor and the rotor with riblets of size and arrangement shown in Table 2. Figure 12a,b show the heat transfer coefficient distribution along the smooth hub surface and surface with riblets, respectively. The figures clearly show the effect of riblets on the heat transfer characteristics along the passage, where riblets tend to increase the heat transfer coefficient, especially in the valley area between two consecutive riblets. To quantify this effect, the area average heat transfer was calculated in both cases. For the hub with riblets, the averaged heat transfer coefficient is 1083 ($W/m^2.k$), while for the smooth hub, it is 1022 ($W/m^2.k$), which means the heat transfer coefficient was increased by around 6% when riblets were added to the hub surfaces. A very similar increment in heat transfer coefficient was reported by Choi et al. [29] when they tested the effect of adding riblets to a straight duct.

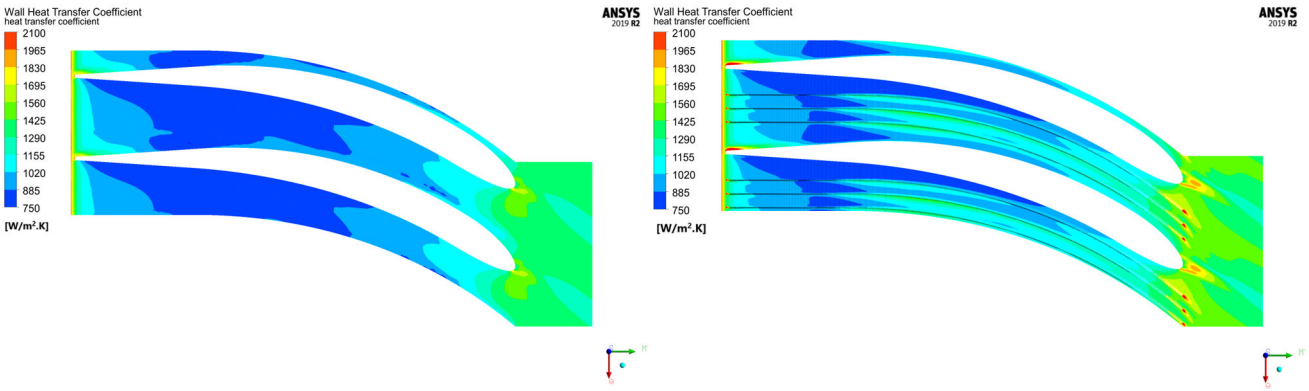

(**a**) (**b**)

Figure 12. (**a**) Heat transfer coefficient over smooth hub, (**b**) heat transfer coefficient over the hub with riblets.

This leap in the heat transfer coefficient urged us to investigate the effect of secondary flows on the heat transport at the hub surface. The normalised flow velocity contours (U/U_c) have been plotted in Figure 13a,b for the smooth rotor passage and passage with riblets, respectively, at the 15% section (refer to Figure 8). The first thing to notice in these plots is that the flow across the passage is almost divided into a jet wake-like flow, where a low velocity flow is concentrated near the pressure surface and the high velocity flow is concentrated near the suction side. This disruption in the flow is caused mainly by pressure difference across the passage, where the fluid contours show the same behaviour as the reduced static pressure ones in Figure 10a. It is of no doubt that part of the momentum transfer happened across the passage is caused by the motion of the secondary flows from the pressure to the suction side, where in Figure 13a the core of the jet flow is larger than that in Figure 13b, reflecting reduction in losses caused by mixing the main stream flow with low velocity secondary flow.

In turbomachinery ducts, both temperature and velocity fields are strongly interlinked, where the velocity field has a strong influence on the temperature distribution [30]. Figure 14 shows the normalised temperature defined as follows:

$$T_n = \frac{T_w - T}{T_w - T_c} \tag{2}$$

where T_n is the normalised temperature, T_w is the wall temperature at the centre of the hub, T_c is the temperature at the centre of the passage, and T is the local temperature. By comparing both Figures 15 and 16, it can be seen that the contour distribution is almost

identical. And in a similar fashion to the velocity, the temperature distribution was affected by the riblets, which means the temperature distribution is affected by the secondary flow motion within the duct. The change in the temperature field due to riblets is not limited to the rotor entry region, as the figures compare the contours at a section located there, but it also exists along the passage. As the comparison in the figures is not quantitative, temperature distribution contours at different sections along the passage have not been plotted to avoid figure redundancy. The change in the temperature field in Figure 13 indicates that the change in the heat transfer coefficient is not confined to the hub surface only, but rather to all the passage surfaces. To quantify this effect, the area average heat transfer was calculated over the blade surface. For the rotor with riblets, the averaged heat transfer coefficient over the blade was found to be 1153 ($W/m^2.k$), while for the blade of the smooth rotor is 1127 ($W/m^2.k$), which means a 2.3% increase due to adding riblets to the rotor hub.

In the next section, the effect of the secondary flow on the thermal boundary layer and the temperature fluctuations along the passage surfaces has been studied to understand the effect of riblets on the heat transfer within the rotor passage.

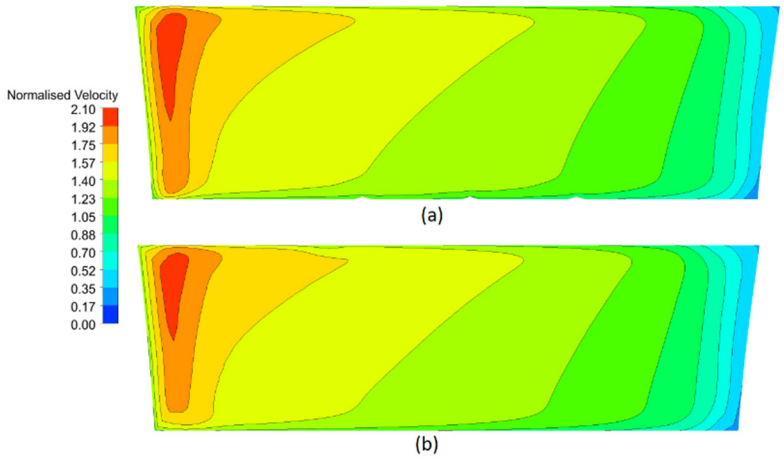

Figure 13. Normalised velocity contours: (**a**) passage with riblets, (**b**) smooth passage.

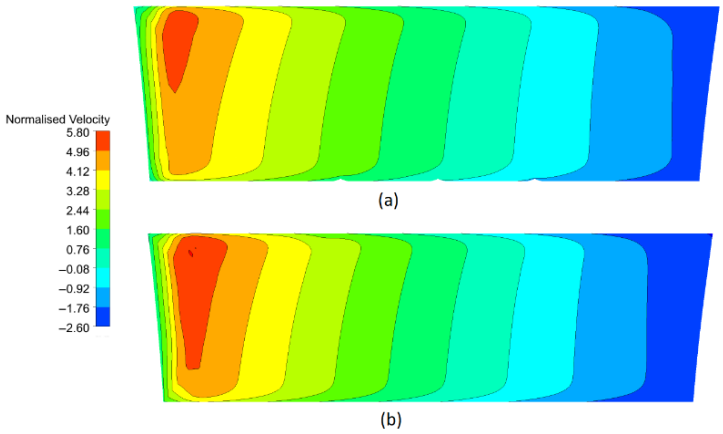

Figure 14. Normalised temperature contours: (**a**) passage with riblets, (**b**) smooth passage.

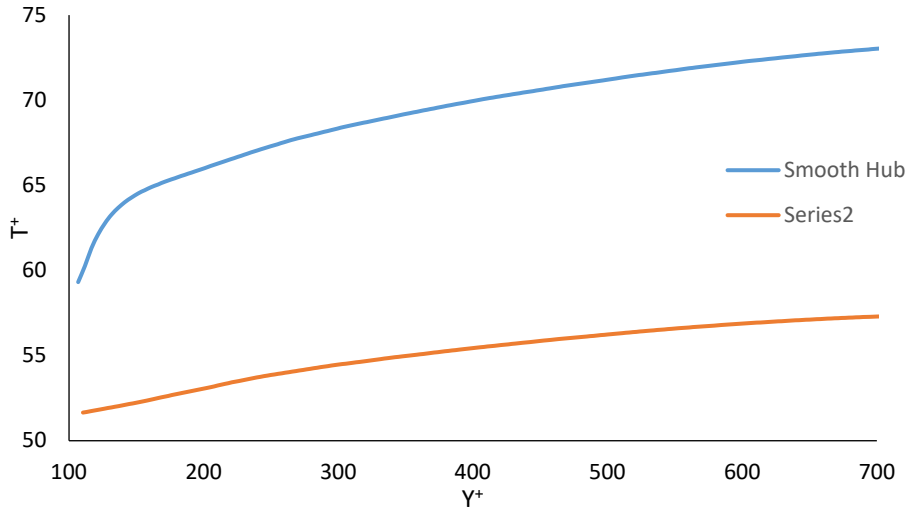

Figure 15. Non-dimensional temperature profile in the spanwise direction located at 44% streamwise sectional plan.

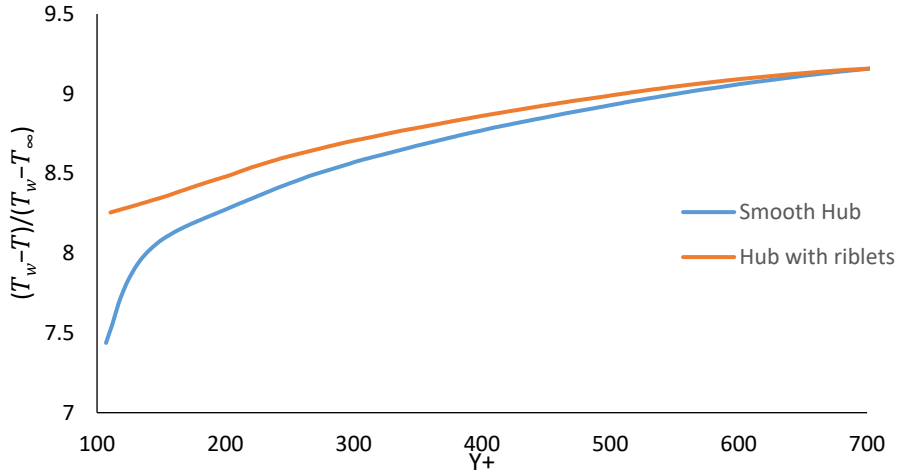

Figure 16. Normalised temperature (temperature gradient) in the spanwise direction located at 44% streamwise sectional plan.

4.3. Thermal Boundary Layer and Temperature Fluctuations

In this section, the virtual origin was considered as the reference to compare the velocity and the thermal boundary layers of the hub surface with riblet with those of a smooth hub. The virtual origin was introduced by many researchers, in different ways, to compensate for the drag caused by various surface roughness [31–33]. The definition that was considered in the work is the one defined by Choi et al. [31], which proves to be more accurate than the other definitions based on the study of Duan et al. [34], who examined the accuracy of different definitions for the virtual origin. In Equation (3), the virtual origin (Y_o) can be evaluated based on the shift in the location of the maximum turbulent kinetic energy.

$$Y_o = Y_m - \frac{Y_m^+ v}{u_\tau^*} \tag{3}$$

where Y_m is the normal distance from the wall to the locations of the maximum turbulent kinetic energy for a smooth surface and Y_m^+ is the same distance but in wall units. u_τ^* is the friction velocity and v is the fluid kinematic viscosity. Figure 15 gives a comparison between the temperature profiles over the hub surface with riblets and over a smooth hub. The comparison was selected at a single section to avoid crowding, and that section is located at 44% of the streamwise length of the passage (refer to Figure 8). The thermal

boundary layer profile was plotted at the middle distance between the pressure and suction surfaces of the passage. The non-dimensional temperature (T^+) plotted in Figure 15 is defined as follows:

$$T^+ = \frac{\rho c_p u_\tau^* (T_w - T)}{h(T_w - T_\infty)} \quad (4)$$

where c_p is the fluid's constant pressure heat capacity, ρ is the density of the fluid, u_τ^* is the friction velocity, h is the convective heat transfer coefficient, T_w is the wall temperature, T_∞ is the free-stream temperature, and T is the local temperature. The shift in the temperature profile due to the existence of riblets was accommodated using the virtual origin distance calculated at each section. The normalised wall distance was defined as

$$Y^+ = \frac{Y u_\tau^* \rho}{\mu}.$$

It is obvious from Figure 15 that adding the riblets to the hub surface results in a significant shift in the temperature profile normal to the surface. This shift suppresses the thickness of the thermal viscous sublayer, which acts as a buffer layer that resists heat transfer. This also indicates that the temperature gradient (Figure 16) at the hub surface increases, leading to a higher heat transfer coefficient.

Figure 17 displays the turbulent kinetic energy (TKE) distribution at the identical axial position previously shown for temperature profiles in Figure 15. The comparative analysis reveals a substantial decrease in TKE over the riblet-textured hub surface compared to the smooth reference case, demonstrating that the surface modifications effectively suppress turbulent velocity fluctuations across all three components. This damping effect reduces momentum exchange between the passage vortex and low-energy near-wall fluid while fundamentally altering turbulent transport mechanisms in the hub region.

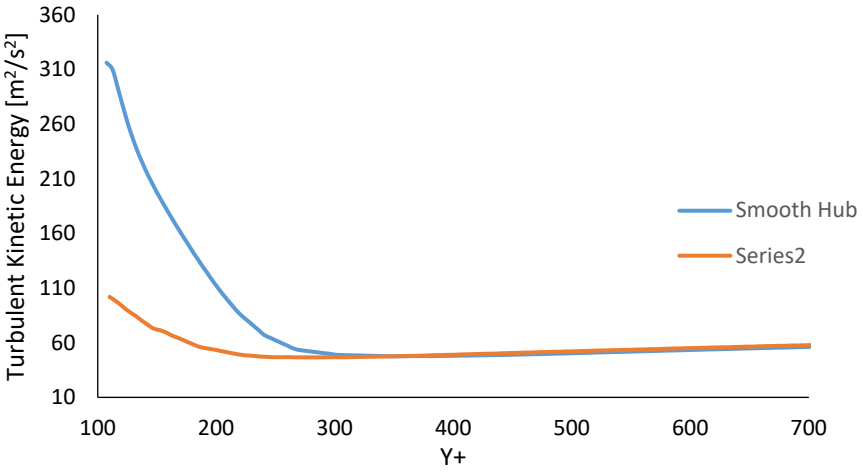

Figure 17. Turbulent kinetic energy in the spanwise direction located at 44% streamwise sectional plan.

Consistent with Reynolds' analogy, this modified momentum transport mechanism necessitates a corresponding increase in heat transfer to maintain the fundamental relationship between momentum and thermal transport within the boundary layer. The riblet-induced reduction in wall friction consequently leads to an elevated heat transfer coefficient, preserving the constant ratio between momentum and heat transfer characteristic of turbulent boundary layers.

These observations align with previous investigations by Puxaun et al. [35], Duan et al. [34], and Lee et al. [36], who similarly reported riblet-mediated modifications to turbulent kinetic energy distributions. The current results extend these findings by demonstrating the coupled aero-thermal effects in the specific context of turbine hub flows.

4.4. Riblets Effect on Thermal Losses

As stated previously, conjugate heat transfer analyses were conducted on a section of the turbine shaft assembly, which will allow the evaluation of the heat transfer from the working fluid through the solid parts of the turbine to the compressor and bearings' housing. This is, eventually, a simplified case, but it will allow us to estimate the impact of riblets on the heat loss from the rotor. The steady-state analysis was performed at the design point condition for the turbine, where boundary conditions for the fluid and solid domains are defined in Figure 18. In this analysis, the shaft surface was defined as perfectly insulated (adiabatic).

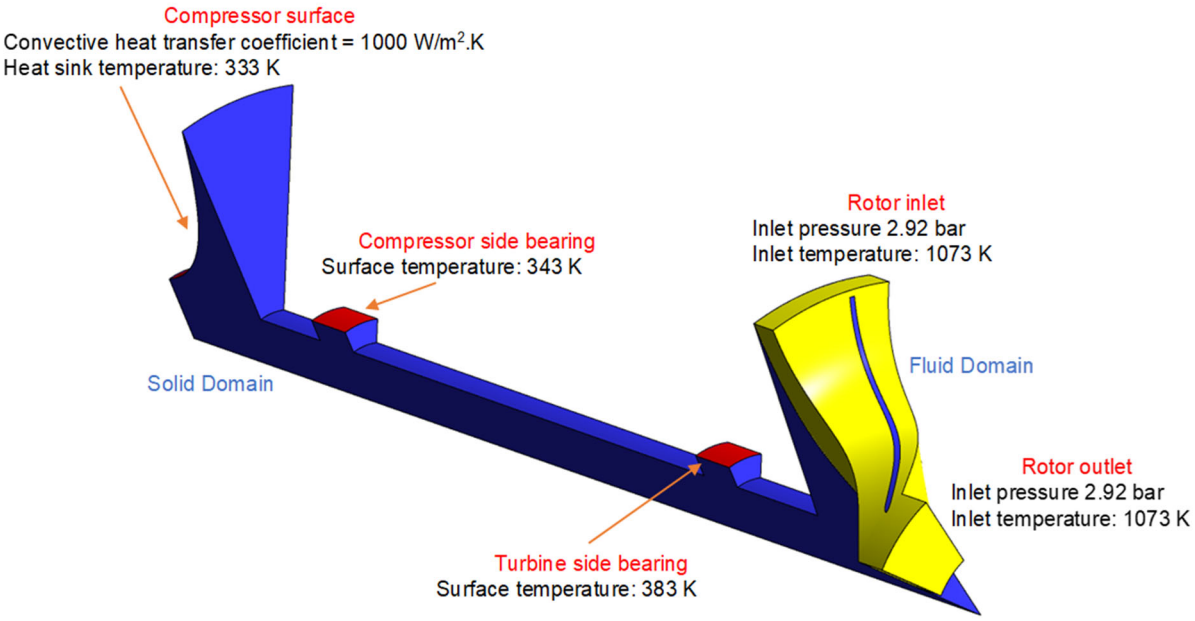

Figure 18. Boundary conditions for the conjugate heat transfer analysis.

The results of the analysis revealed that the rotor heat loss in the case of a smooth hub is 161 Watt, while in the case of a hub with riblets the heat loss is 168 Watt. Thus, adding riblets to the hub increases the heat transfer from the rotor by 4.3%. In both cases, the heat flux through the blades was responsible for 76% of the heat loss, while the flux through the hub contributed to 24% of the heat loss. This result is expected as the area of the blades is 1.8 times larger than the area of the hub; also, the hub is located at the lowest radial point of the rotor, which means it is in contact with the lowest temperature fluid within the passage, resulting in a lower heat transfer rate through its surface than the blade surface.

5. Conclusions

This study employed numerical simulations to evaluate the impact of riblets applied to the hub surface of a radial turbine rotor on convective heat transfer and overall thermal losses. The results demonstrate that riblets increase the heat transfer coefficient by approximately 6% at the hub and 2.3% at the blade surfaces. Although the increase at the blade is smaller, the blade's larger surface area amplifies the total heat transfer effect.

A clear link was established between near-wall turbulent fluctuations and thermal transport. Specifically, reductions in near-wall turbulent kinetic energy (TKE) were associated with enhanced local heat transfer, suggesting a coupled aero-thermal interaction driven by modified secondary flow structures.

Despite the enhancement in heat transfer coefficients, the overall increase in heat loss from the rotor remains modest—approximately 7 W. This reflects the outcome of the steady-

state thermal solution, where the wall temperature closely approaches that of the working fluid, resulting in a minimal temperature gradient and thus limited heat flux. Additionally, the inherently high thermal resistance of the rotor shaft and the relatively small surface area available for heat transfer further constrain thermal losses compared to other micro gas turbine (MGT) components, such as the volute. Nonetheless, modifications to near-wall flow structures significantly influence local thermal behaviour, and their impact becomes increasingly pronounced as machine size increases.

These findings offer a foundation for further exploration into rotor cooling strategies, particularly in the context of advanced additive manufacturing. Tailored surface geometries may enable higher turbine operating temperatures, improved thermal management, and extended component lifetimes.

Author Contributions: M.A.K.: Conceptualisation, Methodology, Validation, Formal Analysis, Investigation, and Writing—Original Draft. A.I.S.: Writing—Review and Editing and Supervision. M.G.: Writing—Review and Editing. J.A.-Z.: Writing—Review and Editing. H.W.: Writing—Review and Editing. All authors have read and agreed to the published version of the manuscript.

Funding: This research received no external funding.

Conflicts of Interest: The authors declare no conflicts of interest.

Nomenclature

Letters	
h	Average heat transfer coefficient ($W/m^2.K$)
k	Thermal conductivity ($W/m.K$)
Y+	Non-dimensional wall distance: $Y^+ = \frac{Yu^*_\tau \rho}{\mu}$
h+	Non-dimensional riblets height: $h^+ = \frac{hu^*_\tau \rho}{\mu}$
u^*_τ	Friction velocity: $\sqrt{\tau_o/\rho}$
τ_o	Wall shear
ρ	Density
T	Temperature (K)
V	velocity
r	Rotor hub radius
PS	Pressure surface of the blade
SS	Suction surface of the blade
Greeks	
μ	Dynamic viscosity (m^2/s)
$\varnothing$	The polar angle between the riblets cusp and the rotor axis
Subscripts	
s	Surface, static
∞	Free-stream fluid
r	Reduced
Abbreviations	
CFD	Computational Fluid Dynamics
CHT	Conjugate Heat Transfer
HSG	High-Speed Generator
MGT	Micro Gas Turbine
RANS	Reynolds-Average Navier–Stokes

References

1. Khader, M.A. Development of a Micro Gas Turbine for Concentrated Solar Power Applications. Ph.D. Thesis, University of London, London, UK, 2017.

2. Khader, M.A.; Sayma, A.I.; Al-Zaili, J.; Ghavami, M. Heat Transfer Effect on Micro Gas Turbine Performance for Solar Power Applications. *Energies* **2021**, *14*, 6745. [CrossRef]
3. Banihabib, R.; Assadi, M. The Role of Micro Gas Turbines in Energy Transition. *Energies* **2022**, *15*, 8084. [CrossRef]
4. Samitha Weerakoon, A.H.; Assadi, M. Micro Gas Turbines in the Global Energy Landscape: Bridging the Techno-Economic Gap with Comparative and Adaptive Insights from Internal Combustion Engines and Renewable Energy Sources. *Energies* **2024**, *17*, 5457. [CrossRef]
5. Proniewicz, M.; Petela, K.; Mouna, C.; Bothien, M.R.; Gruber, A.; Fan, Y.; Lee, M.; Szlęk, A. Preliminary Comparison of Ammonia- and Natural Gas-Fueled Micro-Gas Turbine Systems in Heat-Driven CHP for a Small Residential Community. *Energies* **2025**, *18*, 4103. [CrossRef]
6. Park, J.S.; Park, S.; Kim, M.; Choi, B.S.; Cho, H.H. Effect of Thermal Insulation on Generation and Micro Gas Turbine System. *Elsevier J. Energy* **2013**, *59*, 581–589. [CrossRef]
7. Reale, F.; Massoli, P. A Hybrid Energy System Based on Externally Fired Micro Gas Turbines, Waste Heat Recovery and Gasification Systems: An Energetic and Exergetic Performance Analysis. *Energies* **2024**, *17*, 3621. [CrossRef]
8. De Robbio, R.; Cameretti, M.C.; Agizza, S. Design and Thermo-Economic Analysis of an Integrated Solar Field Micro Gas Turbine Biomass Gasifier and Organic Rankine Cycle System. *Energies* **2023**, *16*, 7050. [CrossRef]
9. Fu, Y.F.; Yuan, C.Q.; Bai, X.Q. Marine drag reduction of shark skin inspired riblet surfaces. *Biosurface Biotribology* **2017**, *3*, 11–24. [CrossRef]
10. Walsh, M. Riblets as a Viscous Drag Reduction Technique. *AAIA J.* **1983**, *21*, 485–486. [CrossRef]
11. Kim, K.; Cho, J.; Kim, J.; Jeong, E. Controlling the Secondary Flows Near Endwall Boundary Layer Fences in a 90° Turning Duct Using Approximate Optimization Method. *J. Mech. Sci. Technol.* **2011**, *25*, 2025–2034. [CrossRef]
12. Miao, X.; Sun, Z.; Zhang, Q.; Atkins, C. End-wall Seconary Flow Control Using Engineering Residual Surface Structure. In Proceedings of the ASME Turbo Expo, Seoul, Republic of Korea, 13–17 June 2016.
13. Oehlert, K.; Seume, J. Exploratory Experiments on Machined Riblets on Compressor Blades. In Proceedings of the ASME Fluids Engineering Division, Miami, FL, USA, 17–20 July 2006.
14. Zhong, J.; Han, J.; Liu, Y.; Tian, F. Numerical Simulation of Endwall Fence on the Secondary Flow in Compressor Cascade. In Proceedings of the ASME Turbo Expo, Berlin, Germany, 9–13 June 2008.
15. Miao, X.; Zhang, Q.; Wang, L.; Jiang, H.; Qi, H. Application of Riblets on Turbine Blade End-wall Secondary Flow Control. *J. Propuls. Power* **2015**, *31*, 1578–1585. [CrossRef]
16. Govardhan, M.; Rajender, A.; Umang, J. Effect of Streamwise Fences on Secondary Flows and Losses in a Two- dimensional Turbine Rotor Cascade. *J. Therm. Sci.* **2006**, *15*, 296–305. [CrossRef]
17. Khader, M.; Sayma, A.I. Effect of End-Wall Riblets on Radial Turbine Performance. In Proceedings of the 10th International Conference on Compressors and their Systems, London, UK, 9–13 September 2017.
18. Khader, M.A.; Sayma, A.I. Drag reduction within radial turbine rotor passages using riblets. *Proc. Inst. Mech. Eng. Part E J. Process Mech. Eng.* **2022**, *236*, 14–25. [CrossRef]
19. Camci, C.; Rizzo, D.H. Secondary Flow and Forced Convectoin Heat Transfer Near EndWall Boundary Layer Fence in 90 Duct. *Int. J. Heat Mass Transf.* **2002**, *45*, 831–843. [CrossRef]
20. Miao, X.; Zhang, Q.; Atkin, C.J.; Sun, Z.; Li, Y. Improving Purge Air Cooling Effectiveness by Engineered End-Wall Surface Structures-Part I: Duct Flow. *J. Turbomach.* **2018**, *140*, 091001. [CrossRef]
21. Miao, X.; Zhang, Q.; Atkin, C.J.; Sun, Z.; Li, Y. Improving Purge Air Cooling Effectiveness by Engineered End-Wall Surface Structures-Part II: Turbine Cascade. *J. Turbomach.* **2018**, *140*, 091002. [CrossRef]
22. Wang, L.; Wang, S.; Wen, F.; Zhou, X.; Wang, Z. Effect of continous wavy ribs on heat transfer and cooling air flow in square single-pass channel of turbine blade. *Int. J. Heat Mass Transf.* **2018**, *121*, 514–533. [CrossRef]
23. Wang, L.; Wang, S.; Wen, F.; Zhou, X.; Wang, Z. Heat transfer and flow characterstics of U-shaped cooling chammels with novel wavy ribs under stationary and rotating conditions. *Int. J. Heat Mass Transf.* **2018**, *126*, 312–333. [CrossRef]
24. Kaewchoothong, N.; Maliwan, K.; Takeishi, K.; Nuntadusit, C. Effect of inclined ribs on heat transfer coefficient in stationary square channel. *Theor. Appl. Mech. Lett.* **2017**, *7*, 344–350. [CrossRef]
25. Davletshin, I.; Mikheev, N.; Dushin, N.; Shakirov, R. Enhancement of transfer processes on a channel wall covered with regular small-size ribs. *Int. J. Therm. Sci.* **2024**, *204*, 109202. [CrossRef]
26. Kumar, M.S.; Abraham, S. Experimental and numerical studies of detailed heat transfer and flow characteristics in the rib turbulated annulus of a double pipe heat exchanger. *Int. J. Therm. Sci.* **2025**, *207*, 109382. [CrossRef]
27. Dai, J.; Ijichi, N.; Tange, H.; Shibata, H.; Tamaki, H.; Yamaguchi, S. Comparison of internal flow field between experiment and computation in a radial turbine impeller. *JSME Int. J.* **2004**, *47*, 48–56. [CrossRef]
28. Wiedner, B.G.; Camci, C. Passage Flow Structure and Its Influence on Endwall Heat Transfer in a 90 deg Turning Duct: Mean Flow and High Resolution Endwall Heat Transfer Experiments. *J. Turbomach.* **1997**, *119*, 39–50. [CrossRef]

29. Choi, K.S.; Hamid, S. Heat transfer Study of Riblets. In *Recent Developments in Turbulence Management*; Kluwer Academic Publishers: Dordrecht, The Netherlands, 1991; pp. 25–41.
30. Lakshminarayana, B. *Fluid Dynamics and Heat Transfer of Turbomachinery*; John Wiley & Sons, Inc.: New York, NY, USA, 1996.
31. Choi, H.; Moin, P.; Kim, J. Direct Numerical Simulation of Turbulent Flow over Riblets. *J. Fluid Mech.* **1993**, *255*, 503–539. [CrossRef]
32. Duan, L. Effects of ribelts on skin friction in high-speed turbulent boundary layers. In Proceedings of the 50th AIAA Aerospace Sciences Meeting and Exhibit, Nashville, TN, USA, 9–12 January 2012.
33. Hopkins, E.J.; Inouye, M. Evaluation of Theories for Predicting Turbulent Skin Friction and Heat Transfer on Flat Plates at Supersonic and Hypersonic Mach Mumbers. *AIAA J.* **1971**, *9*, 993–1003. [CrossRef]
34. Duan, L.; Choudhari, M.M. Effects of Riblets on Skin Friction and Heat Transfer in High-Speed Turbulent Boundary Layers. In Proceedings of the 50th AIAA Aerospace Sciences Meeting including the New Horizons Forum and Aerospace Exposition, Nashville, TN, USA, 9–12 January2012.
35. Puxuan, L.; Campbell, M.; Zhang, N.; Steven, J. Relationship between turbulent structures and heat transfer in microfin enhanced surfaces using large eddy simulations and particle image velocimetry. *Int. J. Heat Mass Transf.* **2019**, *136*, 1282–1298. [CrossRef]
36. Lee, S.J.; Lee, S.H. Flow field analysis of turbulent boundary layer over a riblet surface. *Exp. Fluids* **2001**, *30*, 153–166. [CrossRef]

Disclaimer/Publisher's Note: The statements, opinions and data contained in all publications are solely those of the individual author(s) and contributor(s) and not of MDPI and/or the editor(s). MDPI and/or the editor(s) disclaim responsibility for any injury to people or property resulting from any ideas, methods, instructions or products referred to in the content.